minerals

MDPI

Article

Mesozoic–Cenozoic Multi-Stage Uplift and Exhumation of the Fugu Area, Northeastern Ordos Basin: Constraints from Apatite (U–Th)/He and Fission-Track Thermochronology

Junman Zhang [1], Ming Liang [1], Chuanwei Jia [2], Songsong Cheng [2], Lin Li [1], Chao Wang [1], Xiuyou Xu [1], Chao Niu [3], Lele Xiao [3], Tuo Lu [3], Xiaochen Zhao [3,*] and Yiming Liu [3]

[1] Shaanxi Energy Fengjiata Mining Operation Co., Ltd., Yulin 719400, China
[2] Shandong Energy Group Xibei Mining Co., Ltd., Xi'an 710018, China
[3] College of Geology and Environment, Xi'an University of Science and Technology, Xi'an 710054, China
* Correspondence: zxc@xust.edu.cn

Abstract

As a key component of continental China, the Ordos Basin has experienced long-term overprinting by multiphase tectonism, making it an excellent natural laboratory for investigating intracontinental tectonic evolution. Nevertheless, existing geological studies of the basin show a strong spatial bias: most work focuses on its intensely deformed western and southern domains, whereas systematic data from the northeastern sector remain sparse. This hinders comprehensive reconstruction of the basin's tectono-dynamic evolution. The present study targets the Fugu area in the northeastern Ordos Basin. We conducted systematic apatite fission-track and apatite (U–Th)/He analyses and compiled published regional thermochronological data. These datasets are used to reconstruct the multi-stage uplift and exhumation history of the Fugu area and to decipher evolutionary patterns and underlying dynamic mechanisms. The obtained apatite fission-track and (U-Th)/He ages range from 156.0 ± 8.7 Ma to 182.9 ± 9.6 Ma and 33.58 ± 1.05 Ma to 76.19 ± 2.40 Ma, respectively. Combined with thermal history inverse modeling results, the Mesozoic tectonic evolution of the Fugu area is divided into two stages: initial uplift in the Late Triassic and tectonic exhumation in the Late Jurassic. Further integration with published thermochronological data from the entire northeastern Ordos Basin identifies two additional cooling events during the Late Cretaceous and Paleogene–Neogene. Overall, four major cooling-uplift events have occurred in the northeastern Ordos Basin since the Mesozoic; the Late Cretaceous event is inferred mainly from published records and is not constrained by our new thermochronological results. The results indicate that the Late Triassic uplift was driven by far-field superimposed compression from the final closure of the Paleo-Asian Ocean to the north. The Late Jurassic uplift was closely associated with coeval multi-directional plate convergence on the Ordos Block. In the Late Cretaceous, the study area experienced regional uplift in response to combined subduction of the West Pacific Plate and the Neo-Tethys Ocean and the associated deep continental geodynamic regime. The Paleogene–Neogene rapid exhumation was primarily controlled by eastern Pacific Plate subduction, with supplementary far-field dynamic influences from the northeastward tectonic expansion of the Tibetan Plateau. This study demonstrates that the northeastern Ordos Basin remained tectonically active (rather than quiescent) throughout the Mesozoic, recording multiphase episodic uplift and crustal exhumation. These low-temperature thermochronological constraints help unravel the intracontinental dynamic evolution of the Ordos Basin and refine the regional Mesozoic tectonic evolutionary framework.

Check for updates

Academic Editor: Jim Lee

Received: 9 October 2026
Revised: 24 November 2026
Accepted: 25 November 2026
Published: 29 November 2026

Copyright: © 2026 by the authors. Licensee MDPI, Basel, Switzerland. This article is an open access article distributed under the terms and conditions of the Creative Commons Attribution (CC BY) license.

Keywords: thermochronology; (U-Th)/He; fission track; northeastern Ordos Basin; thermal history; exhumation

1. Introduction

The Ordos Basin, a fundamental geological unit in the western North China Craton (NCC) [1], preserves a comprehensive record of the Mesozoic–Cenozoic tectonothermal evolution, basin–mountain coupling, and intracontinental deformation within the NCC [2–7]. Concurrently, it stands as a prime example of a multi-energy mineral basin in China, characterized by the coexistence and enrichment of coal, petroleum, natural gas, and coalbed methane [5,8,9]. As a typical intra-cratonic relict basin, the Ordos Basin has undergone a complex, multi-stage, and multi-regime tectonic evolution since the Mesozoic [2,10–12]. Precise characterization and systematic reconstruction of this polyphase evolutionary history are of paramount importance. They not only provide critical insights into the reactivation mechanisms of the intracontinental NCC and the far-field responses to intraplate orogeny [1,12], but also establish an indispensable framework for understanding the metallogenesis and hydrocarbon accumulation of the basin's diverse energy resources.

Considerable efforts have been devoted to elucidating the Mesozoic–Cenozoic tectonic evolution of the Ordos Basin and its peripheral orogenic belts, utilizing approaches ranging from stratigraphic contact relationships [13–15] and sedimentary filling signatures [16] to structural deformation analysis and thermochronology [7,17]. These investigations have broadly constrained the overall uplift chronology and evolutionary framework of the basin. A general consensus has emerged that the basin experienced multiple significant phases of uplift and cooling [2,5,7]. However, notable regional heterogeneity exists in the distribution of previous research. The majority of studies have concentrated on the southern [17,18] and western segments of the basin [11,19,20], whereas the northeastern domain, including the Fugu region, remains conspicuously understudied. A comprehensive tectonic evolutionary framework for this critical area has yet to be established, which significantly hampers our holistic understanding of the Ordos Basin's overall tectonic evolution.

The Fugu area lies in the northeastern Ordos Basin, at the transition toward the Jinxi Flexural Fold Belt (JFFB). It has long experienced superimposed tectonic signals from three major tectonic domains: the NCC, the Central Asian Orogenic Belt (CAOB), and the Qinling Orogenic Belt (QOB) [7,21,22]. Its distinctive tectonic position renders the Fugu area highly responsive to multi-stage Mesozoic–Cenozoic tectonism, preserving a relatively complete archive of multi-stage uplift, denudation, and cooling. Compared with the basin interior, this area displays notably more complex tectonic deformation and pronounced differential uplift characteristics [22,23]. Accordingly, its uplift and exhumation history not only serves as a direct proxy for regional tectonic evolution but also constitutes a critical geological factor governing the accumulation, reworking, and preservation of multiple energy minerals [22]. Therefore, accurate determination of the timing, phases, and processes of Mesozoic–Cenozoic uplift and exhumation in the Fugu area is of pivotal significance for elucidating intracontinental deformation mechanisms, basin–mountain coupling, and the energy resource potential along the northeastern margin of the Ordos Basin.

To further advance the understanding of the northeastern Ordos Basin, we present a study of the Fugu area that integrates systematic field investigations and low-temperature thermochronology. Our objectives are to constrain the timing and phases of Mesozoic–Cenozoic uplift and exhumation, interpret their geodynamic drivers and regional tectonic implications, and construct a comprehensive spatiotemporal evolution model. The findings will enrich existing datasets by providing high-precision thermochronological constraints

for the northeastern basin, thereby contributing to the broader understanding of intracontinental reactivation and basin–mountain coupling in the western NCC. In addition, these results will provide essential tectonic guidance for resource assessment, accumulation mechanism studies, and exploration deployment in the Fugu area.

2. Geological Setting

The Ordos Basin, a large polycyclic superimposed basin in the western NCC, is underlain by Archean–Paleoproterozoic crystalline basement and capped by a continuous Cambrian to Quaternary succession. Its evolution spans the Meso-Neoproterozoic aulacogen, Early Paleozoic shallow-marine platform, Late Paleozoic paralic plain, Mesozoic inland lacustrine basin, and Cenozoic peripheral fault depressions [2]. Six first-order tectonic units are recognized based on basement architecture, evolutionary history, and present-day structural configuration: the Yimeng Uplift, Weibei Uplift, Jinxi Flexural Fold Belt, Tianhuan Depression, Yishan Slope, and Western Margin Thrust Belt [24–27]. The basin serves as a major enrichment zone for oil, natural gas, coal, and sandstone-type uranium deposits in China.

The Fugu study area is situated at the junction of the Yimeng Uplift, Jinxi Flexural Fold Belt, and Yishan Slope in the northeastern basin (Figure 1a). Mesozoic–Cenozoic compressional–strike-slip structures are well preserved along fault zones, expressed by low-angle tilting of Paleozoic–Mesozoic strata. Broad gentle flexures and pronounced uplift-exhumation occur toward the northeastern basin margin. Two major faults (the Qingshuichuan Fault and Yushuwan Fault) have been identified. The Qingshuichuan Fault consists of two subparallel normal faults (Zhaiyawan and Luanshita) with ~2.5 km separation, striking ~315° and displaying 1~2 m wide fracture zones with fault breccias. The Yushuwan Fault, striking ~320°, places Lower Permian Shanxi Formation clastics against Lower Ordovician Majiagou Formation limestones. Fault-related folding is evident, with a measured attitude of 225°∠80°. Attitudes of the Middle Permian Lower and Upper Shihezi formations gradually flatten away from the fault (from 230°∠47° to 240°∠15°); the hanging-wall Majiagou Formation maintains a stable attitude of 210°∠12°. The stratigraphic succession in ascending order comprises the Middle Ordovician Majiagou Formation, Upper Carboniferous Benxi and Taiyuan formations, Lower Permian Shanxi Formation, Middle Permian Shihezi Formation, Upper Permian Shiqianfeng Formation, Lower Triassic Liujiagou and Heshanggou formations, Middle Triassic Zhifang Formation, Upper Triassic Yanchang Formation, Lower Jurassic Fuxian Formation, Middle Jurassic Yan'an–Zhiluo–Anding formations, and Quaternary deposits, with the Lower Permian Taiyuan and Shanxi formations being the principal coal-bearing intervals [28].

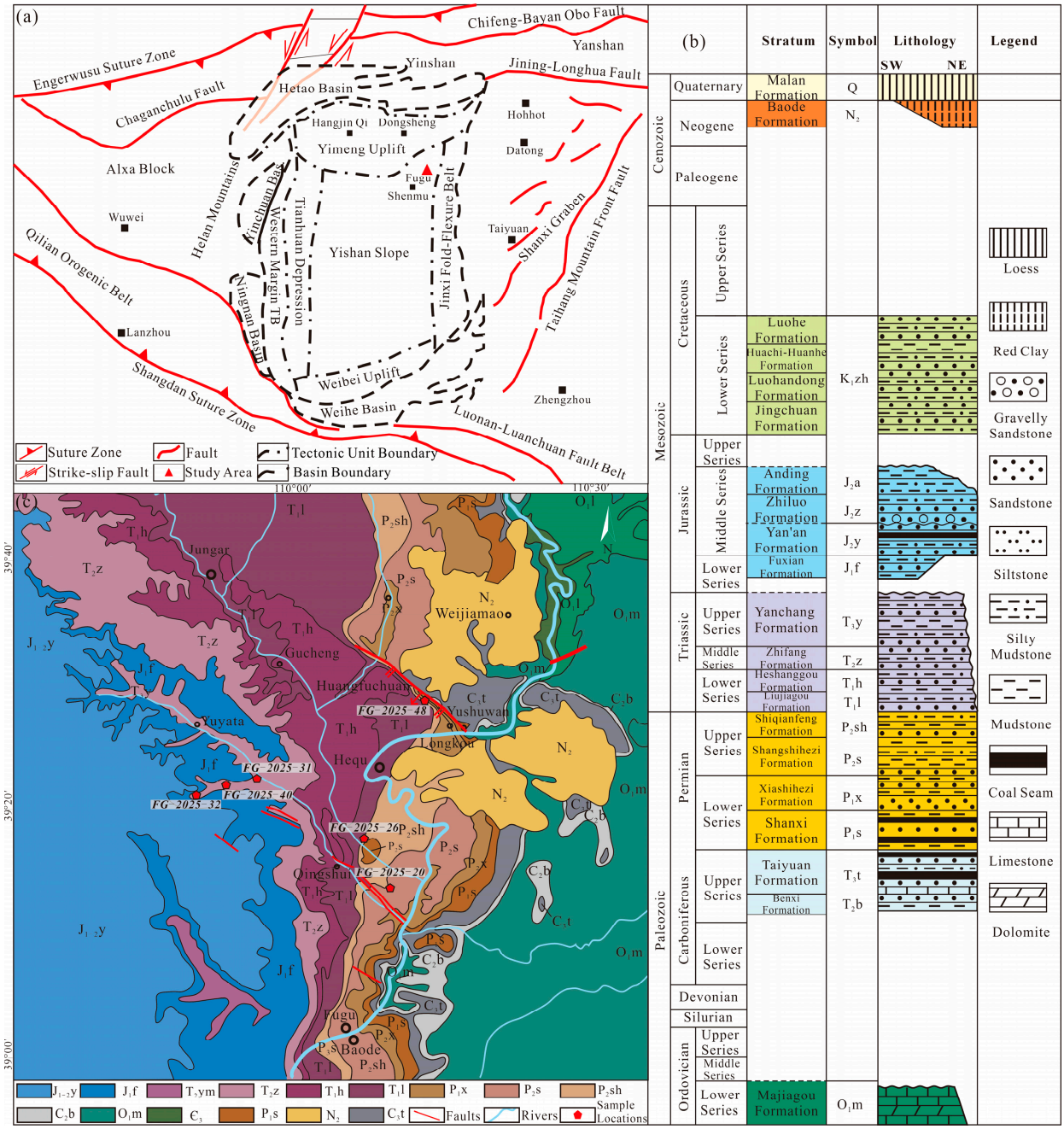


Figure 1. (**a**) Regional tectonic location of the Ordos Basin; (**b**) geological map and sampling locations of the northeastern basin; (**c**) stratigraphic column of the northern Ordos Basin.

3. Sampling and Methods

3.1. Sampling

This study involved the collection of six samples (Table 1), with key information listed below: Sample FG-2025-20 was collected from the northern part of the Shijiacun Gully, 4 km from the Yellow River, with a lithology of grayish-white sandstone of the Shangshihezi Fm. (P_2s); Sample FG-2025-26 was collected from the middle reaches of the Huangfuchuan, with a lithology of grayish-white sandstone of the Shiqianfeng Fm. (P_2sh); Sample FG-2025-31 was collected from a roadside in the Shaqiang area between the Qingshuichuan and the Huangfuchuan, with a lithology of grayish-yellow sandstone of the Zhifang Fm. (T_2z); Sample FG-2025-32 was collected from the Yuyata Gully on the northern side of the Qingshuichuan, with a lithology of grayish-yellow sandstone of the Lower Jurassic

https://doi.org/10.3390/min16121246

Fuxian Fm. (J_1f); Sample FG-2025-40 was collected 0.5 km west of Shenshuwan, with a lithology of grayish-white sandstone of the Zhifang Fm. (T_2z); and Sample FG-2025-48 was collected 0.7 km southwest of Liujiahao, with a lithology of grayish-white sandstone of the Shiqianfeng Fm. (P_2sh).

Table 1. Sample information for this study.

Sample No.	Lithology	Stratigraphic Age	Latitude	Longitude	Altitude
FG-2025-20	sandstone	Shangshihezi Fm.	39°11′36.28″ N	111°08′15.10″ E	891
FG-2025-26	sandstone	Shiqianfeng Fm.	39°15′43.23″ N	111°07′40.09″ E	872
FG-2025-31	sandstone	Zhifang Fm.	39°19′31.66″ N	111°01′04.57″ E	974
FG-2025-32	sandstone	Fuxian Fm.	39°18′01.44″ N	110°55′05.91″ E	1063
FG-2025-40	sandstone	Zhifang Fm.	39°19′3.92″ N	110°58′35.06″ E	1004
FG-2025-48	sandstone	Shiqianfeng Fm.	39°27′32.76″ N	111°14′34.16″ E	1032

3.2. Methods

Low-temperature thermochronology mainly refers to radiometric dating systems with closure temperatures (partial annealing zones, PAZ) below approximately 300 °C, including zircon (U–Th)/He (ZHe), apatite fission track (AFT), and apatite (U–Th)/He (AHe) [29,30]. As advanced and robust analytical tools, low-temperature thermochronological methods have been broadly utilized in multiple geological research fields. It plays a crucial role in geological chronology determination [31,32], constraining the tectonic evolution of orogenic belt [33,34], reconstructing thermal evolution of sedimentary basins [35], analyzing landscape evolution [36,37], and tracing sediment provenance [38,39]. In this study, apatite fission-track and (U-Th)/He dating were applied to decipher the tectonic evolution of the Fugu area, northeastern Ordos Basin. The AFT system responds to thermal perturbations over ~60–120 °C, known as the partial annealing zone (PAZ), equivalent to burial depths of roughly 2–4 km within the upper crust [40]. By comparison, AHe can reconstruct time–temperature histories for thermal conditions between ~40 and 85 °C [41,42].

The AFT analyses were completed at Nanjing Hongchuang Geological Exploration Technology Service Co., Ltd. The grinding and polishing were performed using a PRESI MECATECH SP300 (manufacturer, city, state abbreviation if USA or Canada, country). The mount was polished sequentially with 6 µm, 3 µm, and 0.5 µm diamond suspensions to expose the interior surface of the grain, remove scratches, and achieve a flat surface. Mounts were etched in 5 M HNO_3 at 21 °C for 20 s. Apatite grains with polished surfaces parallel to prismatic crystal faces and homogeneous track distributions were selected using a Zeiss Axio Imager Z2m microscope [43,44]. Fission-track analyses adopted the Autoscan System [45]. The Track-Works software (version 3) was used to capture stacks of high-resolution digital images with a ×100 dry objective under both transmitted and reflected light using a highly sensitive and fast iDS camera. Confined tracks were manually counted in FastTracks using coincidence mapping [46], with ROIs predefined for track-density quantification. Tracks were identified by linear transmitted-light traces and reflected-light etch pits. Dpar values were measured simultaneously as kinetic parameters for thermal modeling. The length of the confined fission track was selected from the track-in-track (TINT). After fission-track analysis, the mount was transferred into a LA-ICP-MS system (Laser Ablation Inductively Coupled Mass Spectrometer) for ablation using a 33 µm pit to measure U, Th, Sm, and Pb, as well as a range of trace elements if desired. Each measurement consisted of a 10 s background measurement followed by 35 s of ablation at 8 Hz using a fluence of 2.5 J/cm^2 and a 25 s washout period. For element concentration measurements, NIST SRM 610 glass was used as the calibration reference material, with 43Ca used for internal normalization. NIST SRM 612 glass served as secondary standards for element checks. Apatite fission-track

ages were calculated using the zeta-calibration method, and the zeta value was calibrated against international age standards.

Apatite (U–Th)/He dating was performed at the Isotope Thermochronology Laboratory, Institute of Geology, Chinese Academy of Geological Sciences. Apatite grains separated from rock samples were further screened under a binocular stereomicroscope. Well-formed crystals were preferentially selected, whereas grains containing inclusions were excluded where possible. Crystal dimensions were measured using an ocular micrometer, and the α-ejection correction factor [47] was calculated accordingly. After dimensional measurement, photomicrographs of selected crystals were acquired, and individual grains were loaded into platinum capsules. Helium was extracted by diode-laser heating, and the $^{4}He/^{3}He$ ratio was determined using an Alphachron^{TM} helium isotope mass spectrometer. The ^{4}He abundance was quantified by isotope dilution, with measurement uncertainty < 1%. Following He analysis, grains were chemically dissolved, and their U and Th concentrations were determined by inductively coupled plasma mass spectrometry (ICP-MS). The analytical uncertainties for U and Th isotopic ratios were less than 1% [48]. Finally, the (U–Th)/He ages were calculated from the measured ^{4}He, ^{238}U and ^{232}Th abundances.

4. Results

4.1. AFT Data

Apatite fission-track (AFT) dating analyses were performed on three samples in this study. Our new AFT data are presented in Table 2. Only one sample (FG-2025-26) passed the χ^2 test [$P(\chi^2) > 5\%$], suggesting a single-grain age population. By contrast, two samples (FG-2025-31, FG-2025-32) with $P(\chi^2) < 5\%$ failed the χ^2 test. Sample FG-2025-26 yielded 31 single-grain AFT ages, with a central age of 182.9 ± 9.6. Sample FG-2025-31 yielded 27 single-grain AFT ages. These ages can be split into two populations of 115.0 Ma (P1) and 216.0 Ma (P2). Sample FG-2025-32 gives 36 single-grain AFT ages, which are decomposed into two populations of 118.0 Ma (P1) and 220.0 Ma (P2).

Table 2. Apatite fission-track analysis results of the northeastern Ordos Basin.

Sample No.	Lithology	N	^{238}U (ppm)	ϱ_s ($10^5/cm^2$) (N_s)	n	MTL (μm)	SD	D_{par} (±1σ) (μm)	Central Age (±1σ) (Ma)	P1 (Ma ± 1σ) (%)	P2 (Ma ± 1σ) (%)	P (χ^2)/%
FG-2025-26	sandstone	31	14.91	13.01 (1935)	94	10.92	1.73	1.94	182.9 ± 9.6	/	/	22
FG-2025-31	sandstone	27	17.66	13.56 (2093)	100	10.79	1.48	1.95	176.0 ± 16.0	115.0 ± 10.0 43%	216.0 ± 17.0 57%	0
FG-2025-32	sandstone	36	14.72	11.18 (2375)	100	10.95	1.56	1.80	156.0 ± 8.7	118.0 ± 5.7 77%	220.0 ± 26.0 23%	0

Note: N, number of individual apatite grains; ϱs, apatite fission-track density; Ns, number of spontaneous tracks; n, number of measured track lengths; MTL, mean confined track length; SD, standard deviation of confined track lengths; Dpar, maximum diameter of the fission-track etch figure parallel to the crystallographic C-axis and intersecting the polished surface; $P(\chi^2)$: probability of obtaining χ^2-test value, a probability > 5% is indicative of a homogenous population; Binomial peak fitted ages (P1-P2) were processed by IsoplotR (version 7.2).

The mean track lengths vary from 10.79 ± 1.48 to 10.95 ± 1.56 μm, and track-length distributions are predominantly unimodal. All measured track lengths are shorter than the unannealed initial fission-track length (16.3 ± 0.9 μm), indicating substantial thermal annealing. The observed track shortening constrains a protracted residence of the samples within the PAZ after their deposition, succeeded by a phase of comparatively rapid cooling and exhumation out of the PAZ. All samples yield tightly clustered Dpar values between 1.80 μm and 1.95 μm, reflecting negligible compositional differences in apatite grains from the study area. We therefore infer that dispersion in AFT ages and track lengths is primarily controlled by tectonothermal evolution, rather than apatite geochemistry [20].

4.2. AHe Data

Apatite (U-Th)/He dating results from sedimentary sequences commonly display prominent age dispersion [49,50]. Such scattered ages are governed by multiple complex mechanisms, primarily including accumulated radiation damage within minerals [30,51], occurrence of U-Th-rich inclusions inside individual grains [52], overprinting of externally implanted helium [53], compositional heterogeneity among single crystals [54], and post-depositional modification induced by grain fragmentation [55].

In this study, (U-Th)/He dating analyses were performed on a total of 15 single apatite grains from three samples (Table 3). Each sample was dated using five apatite crystals. Moderate reproducibility is observed in the measured ages, consistent with their detrital provenance. Within each group of tested grains, 2~3 analyses form tight age clusters, supporting the determination of sample-averaged ages. Given the generally dispersed nature of AHe ages, additional outliers were identified using the Hampel identifier with a threshold of four [33,56]. The remaining single-grain AHe ages ranged from 24.73 ± 1.46 Ma to 143.04 ± 8.47 Ma, with central ages ranging from 33.58 ± 1.05 Ma to 76.19 ± 2.40 Ma. For sample FG-2025-20, the apatite (U-Th)/He ages of five analyzed grains range from 86.76 ± 5.12 Ma to 24.73 ± 1.46 Ma, yielding a weighted mean age of 33.58 ± 1.05 Ma after outlier removal. Five apatite grains separated from sample FG-2025-40 record (U-Th)/He ages varying between 37.84 ± 2.49 Ma and 131.42 ± 7.64 Ma; their weighted mean age is calculated as 58.11 ± 1.90 Ma once outliers are excluded. The measured apatite (U-Th)/He ages of five grains from sample FG-2025-48 span 54.91 ± 3.28 Ma to 577.03 ± 35.21 Ma, with a weighted mean age of 76.19 ± 2.40 Ma following the elimination of anomalous data points.

Effective uranium concentration (eU = U + 0.235 × Th) is adopted to quantify the integrated radiogenic production from U and Th decay [29,30,51]. eU (ppm, 1 ppm = 1 μg/g) is widely applied to reflect the degree of α-radiation damage [51], and elevated eU values are generally linked to enhanced He diffusivity [57]. In this study, all 15 analyzed apatite grains yield eU values below 600 ppm (Figure 2, Table 3), implying negligible effects of radiation-induced He diffusion amplification [57]. The AHe ages of the samples show no clear linear correlation with eU or the radius of grains (Figure 2a,b), suggesting that the samples are not strongly affected by radiation damage. Additionally, representative apatite and zircon grains show euhedral to subhedral habits under optical microscopy. Grains with abundant U-Th-rich inclusions or fractures were rigorously excluded during mineral separation.

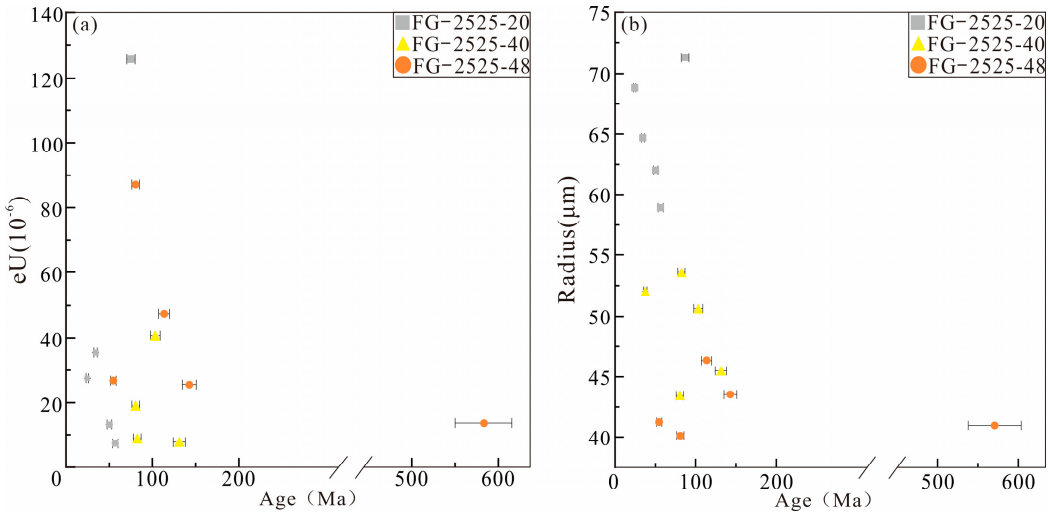


Figure 2. Single-grain AHe age–eU (**a**) and AHe age–grain size (**b**) plots.

Table 3. Apatite U-Th/He analysis results of the northeastern Ordos Basin.

Sample No.	Grain Length (μm)	Grain Width (μm)	4He (ncc)	1σ	U ($\times 10^{-6}$)	1σ	Th ($\times 10^{-6}$)	1σ	Th/U	FT	eU	Corrected Age (Ma)	1σ (Ma)	Radius (μm)	Mass (μg)
FG-2025-20-1	200.9	141.3	0.4983	0.0127	13.21	0.36	60.83	1.54	4.72	0.77	27.51	24.73	1.46	68.82	7.86
FG-2025-20-2	163.5	156.7	0.5975	0.0151	30.65	0.70	20.25	0.43	0.68	0.76	35.41	34.52	2.05	64.62	5.28
FG-2025-20-3	176.1	135.9	0.3443	0.0087	7.63	0.17	23.83	0.45	3.20	0.74	13.23	50.59	2.93	62.01	5.68
FG-2025-20-4	154.5	124.3	0.1722	0.0044	5.21	0.17	9.43	0.27	1.86	0.74	7.43	56.85	3.46	58.99	4.56
FG-2025-20-5	255.8	140.2	8.7320	0.2204	107.40	2.38	76.35	1.45	0.73	0.79	125.34	86.76	5.12	71.28	8.40
												33.58	**1.05**		
FG-2025-40-1	111.3	104.1	0.2227	0.0056	15.10	0.35	16.06	0.34	1.09	0.65	18.87	80.42	4.74	43.49	1.87
FG-2025-40-2	139.1	106.1	0.2362	0.0060	10.51	0.51	65.17	3.17	6.36	0.69	25.83	37.84	2.49	52.05	2.88
FG-2025-40-3	125.0	99.1	0.1667	0.0042	3.98	0.09	13.67	0.27	3.53	0.65	7.19	131.42	7.64	45.50	2.22
FG-2025-40-4	129.8	106.5	0.2145	0.0054	3.35	0.07	23.90	0.47	7.32	0.70	8.97	82.56	4.78	53.57	3.41
FG-2025-40-5	129.1	110.7	1.0326	0.0263	32.79	0.78	33.89	0.74	1.06	0.70	40.76	103.26	6.12	50.64	2.89
												58.11	**1.90**		
FG-2025-48-1	148.4	96.7	0.1602	0.0040	25.39	0.58	5.81	0.13	0.23	0.64	26.75	54.91	3.28	41.21	1.41
FG-2025-48-2	144.1	91.4	0.8519	0.0213	37.39	0.90	42.96	0.91	1.18	0.67	47.48	113.97	6.73	46.35	1.94
FG-2025-48-3	129.0	85.4	0.6582	0.0165	68.06	1.49	80.78	1.52	1.22	0.62	87.04	80.93	4.73	40.12	1.25
FG-2025-48-4	134.3	91.3	0.4554	0.0114	21.85	0.50	15.49	0.30	0.73	0.65	25.49	143.04	8.47	43.52	1.58
FG-2025-48-5	128.2	95.5	0.8005	0.0202	13.11	0.32	1.97	0.07	0.15	0.63	13.57	577.03	35.21	40.93	1.29
												76.19	**2.40**		

Note: The bold numbers in the table denote mean ages obtained after removing discrete age outliers.

4.3. Thermal History Modeling

Based on measured apatite fission-track (AFT) ages, confined track lengths, Dpar values and radiation damage proxies, we conducted thermal-history inverse modeling of thermochronological data. AFT thermal inversion was restricted exclusively to sample FG-2025-26, which yielded $P(\chi^2) > 5\%$. Apatite (U-Th)/He ages exhibit large dispersion, and multi-grain joint inversion fails to yield valid thermal-history solutions. Accordingly, we selected single grains whose ages are closest to the weighted mean age of each sample for thermal-history modeling. Thus, three apatite grains (FG-2025-20-3, FG-2025-40-1 and FG-2025-48-3) were selected for apatite (U-Th)/He (AHe) modeling. Input parameters for each grain included U and Th concentrations, equivalent radius, and uncorrected age. Model parameters were configured as follows: the calibration scheme (Durango apatite standard) was used [58], and α-ejection age correction followed [59]. AHe age modeling was performed using the radiation-damage accumulation and annealing model proposed by Flowers et al. [30]. All thermal-history simulations were run using HeFTy software (version 1.9.1). This software and its underlying inverse modeling framework are described in [60].

The following constraints were implemented: (1) the full annealing time limit was set to be older than both the maximum single-grain age of the sample and the oldest depositional age of the strata; (2) the initial low-temperature boundary conditions were

constrained to match the sedimentary and exhumation stages of the strata; (3) modeled thermal evolution paths must pass through the partial annealing zone within the range of the corresponding sample AFT ages; (4) the present-day average surface temperature of 20 ± 5 °C was adopted as the terminal constraint for modeling; and (5) the initial confined track length was assigned as 16.3 μm [40]. In this study, the prior constraints were set broadly, without overimposing restrictive geological assumptions. The goodness-of-fit (GOF) statistic was employed to evaluate the consistency between the model predictions and the observed data. In the resulting thermal history plots, green envelopes represent acceptable paths (GOF > 0.05), pink envelopes denote good-fit paths (GOF > 0.50), the black line indicates the best-fit path, and the yellow line represents the weighted mean path. The consistently high GOF values for both AFT ages and track length distributions (all exceeding 0.50) indicate that the modeling results are statistically robust and reliable.

Sample FG-2025-26 records multi-stage uplift events: (1) a prominent cooling episode initiated at ca. 230 Ma starting from ~100 °C, followed by temperature reduction to ~60 °C by ca. 180 Ma; (2) then remained at temperatures of 40 °C~60 °C for a prolonged interval; and (3) rapid cooling resumed at ~20 Ma and continued until the present-day surface temperature of ~20 °C was attained (Figure 3).

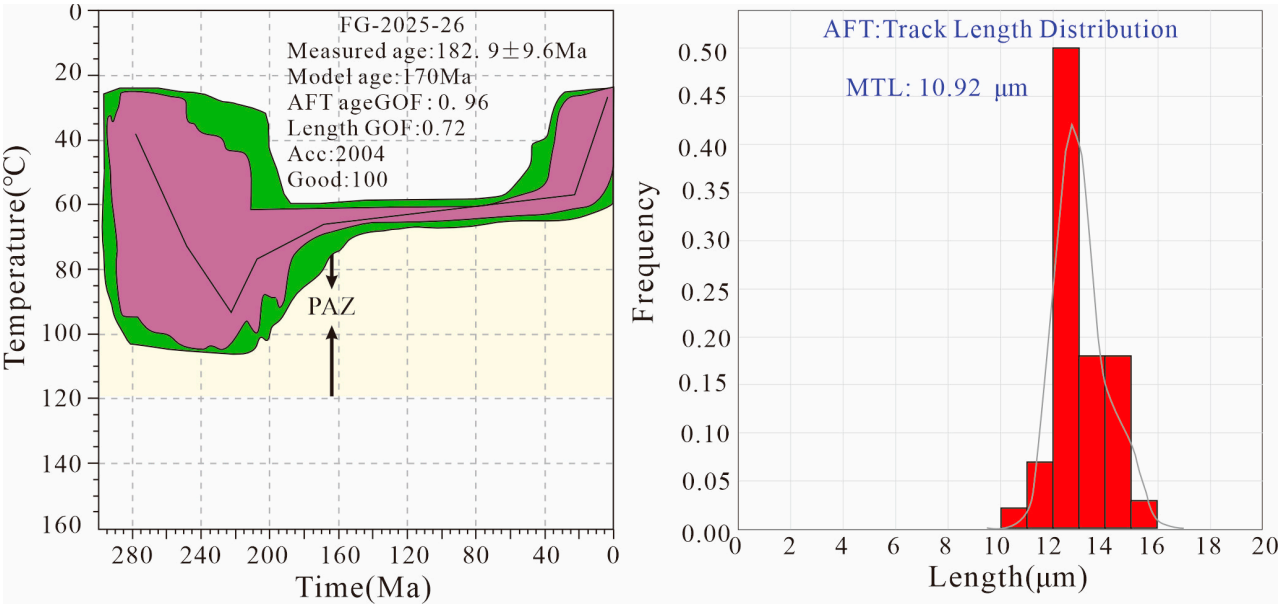


Figure 3. AFT modeling result of sample FG-2025-26 in the northeastern Ordos Basin.

Sample FG-2025-20-3 records multi-stage uplift events: (1) a prominent cooling episode initiated at ca. 200 Ma starting from ~120 °C, followed by temperature reduction to ~80 °C by ca. 150 Ma, and (2) then remained at temperatures of 60 °C~80 °C for a prolonged interval (Figure 4).

Sample FG-2025-40-1 records multi-stage uplift events: (1) a prominent cooling episode initiated at ca. 160 Ma starting from ~90 °C, followed by temperature reduction to ~70 °C by ca. 120 Ma, and (2) then remained at temperatures of 60 °C~80 °C for a prolonged interval (Figure 4).

Sample FG-2025-48-3 records multi-stage uplift events: (1) a prominent cooling episode initiated at ca. 220 Ma starting from ~120 °C, followed by temperature reduction to ~50 °C by ca. 120 Ma, and (2) then remained at temperatures of 40 °C~60 °C for a prolonged interval (Figure 4).

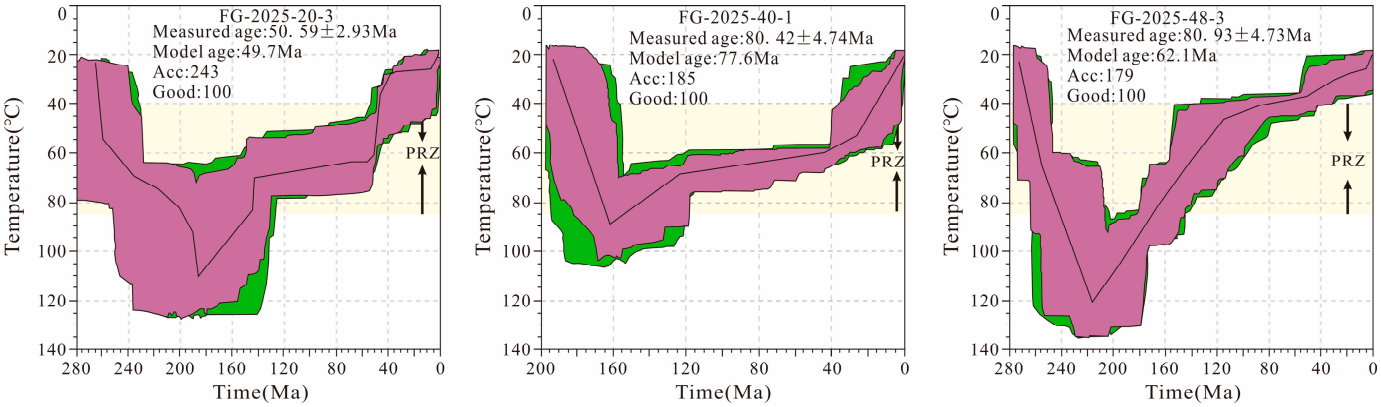


Figure 4. U-Th-He modeling results of samples in the northeastern Ordos Basin.

5. Discussion

5.1. Uplift and Exhumation History of the Fugu Region

Integrating apatite fission-track and (U-Th)/He dating results, thermal inversion modeling outputs, and structural deformation features within the Fugu area, this study reconstructs the Mesozoic–Cenozoic uplift and exhumation evolution of the study area. Thermochronological modeling outcomes for the Fugu area reveal an initial cooling and uplift episode in the Late Triassic; nevertheless, this thermal signal is only captured in the inverse thermal paths and peak ages of several individual specimens (FG-2025-31). This tectonic event produced distinct geological responses in the northeastern Ordos Basin. A typical case is the extensive angular-parallel unconformity in the northeastern Ordos Basin between the Lower–Middle Jurassic Yan'an Formation ($J_{1–2}y$) and Middle–Late Triassic strata (the Yanchang Formation (T_3y) and Zhifang Formation (T_2z)). Moreover, in the eastern part of Jungar Banner, the Middle Jurassic Yan'an Formation ($J_{1–2}y$) rests unconformably directly upon the Upper Permian Shiqianfeng Formation (P_2sh), with the entire Triassic succession absent. Collectively, these lines of evidence indicate that the northeastern Ordos Basin experienced a relatively intense compressional uplift event at the end of the Late Triassic. This event resulted in extensive denudation of the Upper Triassic strata and the development of widespread stratigraphic unconformities across the region.

The second cooling-uplift event occurred in the Late Jurassic, with thermochronological cooling initiated at 180~160 Ma. Subsequent to this uplift phase, all studied samples cooled to temperatures beyond the upper boundary of the apatite partial annealing zone (PAZ) and entered a prolonged period of tectonothermal quiescence. The Middle Jurassic Zhiluo (J_2z) and Anding formations (J_2a) are well preserved across most areas of the northern basin with no significant denudation, whereas Upper Jurassic strata (J_3) are entirely absent. The northern basin margin experienced intensive compressional deformation during the Late Jurassic. Field outcrops reveal that Triassic–Jurassic strata were subjected to tilting and uplift (Figure 4) and exhibit an angular unconformable contact with the overlying Lower Cretaceous. Seismic data further demonstrate the presence of this unconformity between the Middle Jurassic and Lower Cretaceous strata (J_2/K_1) within the northeastern Ordos Basin. Collectively, these lines of evidence indicate that significant tectonic uplift affected the northeastern Ordos Basin during the Late Jurassic.

Two apatite fission-track samples from this study yield tightly clustered late Early Cretaceous ages of 115.0 Ma and 118.0 Ma. These ages are younger than the depositional ages of the host strata, ruling out the possibility of detrital source-area ages and indicating a post-depositional thermal signal. The single-grain ages of this component show tight clustering and low dispersion, consistent with the characteristics of a post-depositional

cooling signal. The widespread absence of strata ranging from the late Early Cretaceous to the entire Late Cretaceous in the northeastern Ordos Basin represents the geological response to this phase of regional uplift and exhumation. Published thermochronological data from surrounding areas support a regional cooling event in the late Early Cretaceous as well (e.g., [22,61]).

Furthermore, we obtained several single-grain (U–Th)/He ages of the Paleogene interval. Previous studies have suggested rapid exhumation and cooling within the Ordos Basin since the late Cenozoic. The eastern sector experienced uplift at a rate of 95 m/Ma, corresponding to ~2000 m of denudation [2,62,63]. This event is generally attributed to the far-field effects of Tibetan Plateau uplift [22]. It should be emphasized that this Cenozoic cooling trend is constrained by only a small set of single-grain AHe ages and AFT thermal-history models, and further independent thermochronological data are required to better resolve its timing.

5.2. Uplift Events of the Northeastern Ordos

Integrating our new analytical results with published low-temperature thermochronological datasets from the northeastern Ordos Basin, we reconstruct the Mesozoic tectonic uplift framework for this region (Figure 5, Table 4). We adopted the following criteria for data compilation and screening: (1) according to the $P(\chi^2)$ test value, age data since 230 Ma were selected for discussion, and age data possibly reflecting the cooling history of source-area uplift were excluded (e.g., single-grain ages significantly older than the stratigraphic depositional age); (2) to clarify the uplift evolution characteristics of different segments in the study area, data without specific sample locations were temporarily excluded from this discussion; and (3) if $P(\chi^2) > 5\%$, the pooled age is used for interpretation. If $P(\chi^2) < 5\%$, the peak age from Gaussian fitting is prioritized; the central age serves as a secondary option. According to the above criteria, a total of 97 valid analytical data were integrated, including 74 apatite fission-track ages (including 17 fitted ages), 20 zircon fission-track ages (including 11 fitted ages), and 3 (U-Th)/He ages (Supplementary Table S1). After removing entries that failed the screening criteria, 86 groups of valid data were ultimately used for tectonic event analysis.

Table 4. Characteristics of tectonic episodes in the northeastern Ordos Basin.

Tectonic Episode	Sedimentary Feature	Contact Relationship	Low-Temperature Thermochronological Data	Tectonic Setting
Paleogene–Neogene	Brick-red mudstone or strata absent	Low-angle unconformity	65.0~12.0 Ma	Subduction and convergence of the Pacific Plate and the India–Eurasia collision
Late Cretaceous	Strata absent	Paraconformity	98.0~66.0 Ma	Subduction of western Pacific and Neo-Tethys
Late Jurassic	Strata absent	Angle unconformity	156.0~141.0 Ma	Multi-directional plate convergence
Late Triassic	Sandstone–mudstone	Angular unconformity	224.2~203.0 Ma	Closure of the Paleo-Asian Ocean

The statistical results show that the northeastern Ordos Basin mainly has the following age concentration intervals: Late Triassic (224.2~203.0 Ma), Late Jurassic–Earliest Cretaceous (156.0~141.0 Ma), Late Cretaceous (98.0~66.0 Ma), and Paleogene–Neogene

(65.0~12.0 Ma). Combined with regional stratigraphic and tectonic data, the above fission-track age concentration intervals all have obvious geological responses.

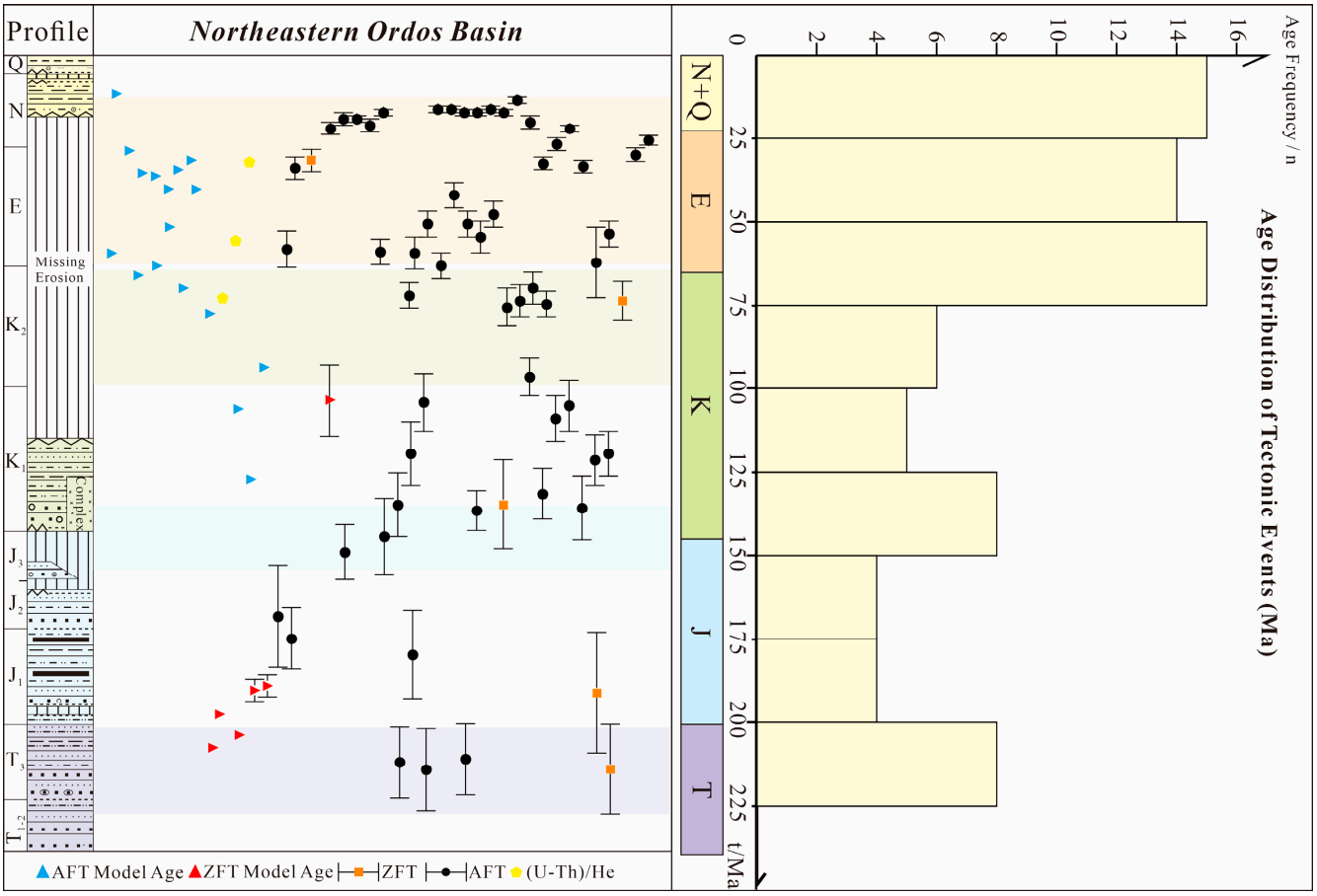


Figure 5. Mesozoic–Cenozoic low-temperature thermochronological sequence in the northeastern Ordos Basin and its correlation with unconformity-related tectonic events.

During the Late Triassic, a NW-trending compressional deformation structure developed in the northeastern Ordos Basin. Field investigations show that the Triassic strata in the Fugu–Dongsheng area of the northeastern basin experienced strong erosion, and widespread contemporaneous unconformities developed regionally (e.g., Wuziwan in Jungar Banner, Hazhen and Mazhen in Fugu) (Figure 6). Lithofacies and thickness variations in the Triassic Yanchang Formation (T_3y) further suggest that this unit was originally deposited over a broader area with greater thickness and subsequently suffered substantial erosion in its northeastern domain. The structural deformation in the Fugu–Jungar Banner area is NW-SE trending, with strata dipping to the west and southwest, and the erosion thickness increasing from southwest to northeast, indicating that the compressional stress was derived from the northeast. At present, the absence of the Yanchang Formation along the Dongsheng–Fugu line to the northeast should represent the erosional boundary, and the inferred erosion amount may exceed 1000 m.

From the Late Jurassic to Early Cretaceous, tectonic deformation and uplift mainly occurred along the northern margin of the basin, while the rigid block in the basin interior was weakly affected by tectonic movement. The northern margin of the basin experienced strong compressional deformation; the Upper Paleozoic coal-bearing strata were thrust to near the surface, and the Triassic–Jurassic strata were tilted and uplifted, showing an angular unconformity with the overlying Early Cretaceous strata (Figure 6). However, this

angular unconformity transitions into a parallel unconformity several kilometers farther north toward the basin margin. This implies that compressional tilting was restricted to a narrow zone within a few kilometers of the basin's northern margin, with no substantial uplift or deformation across the central–southern Yimeng Uplift. Moreover, the Middle Jurassic Zhiluo–Anding Formations in the Yimeng Uplift within the basin interior are well preserved and did not experience strong erosion.

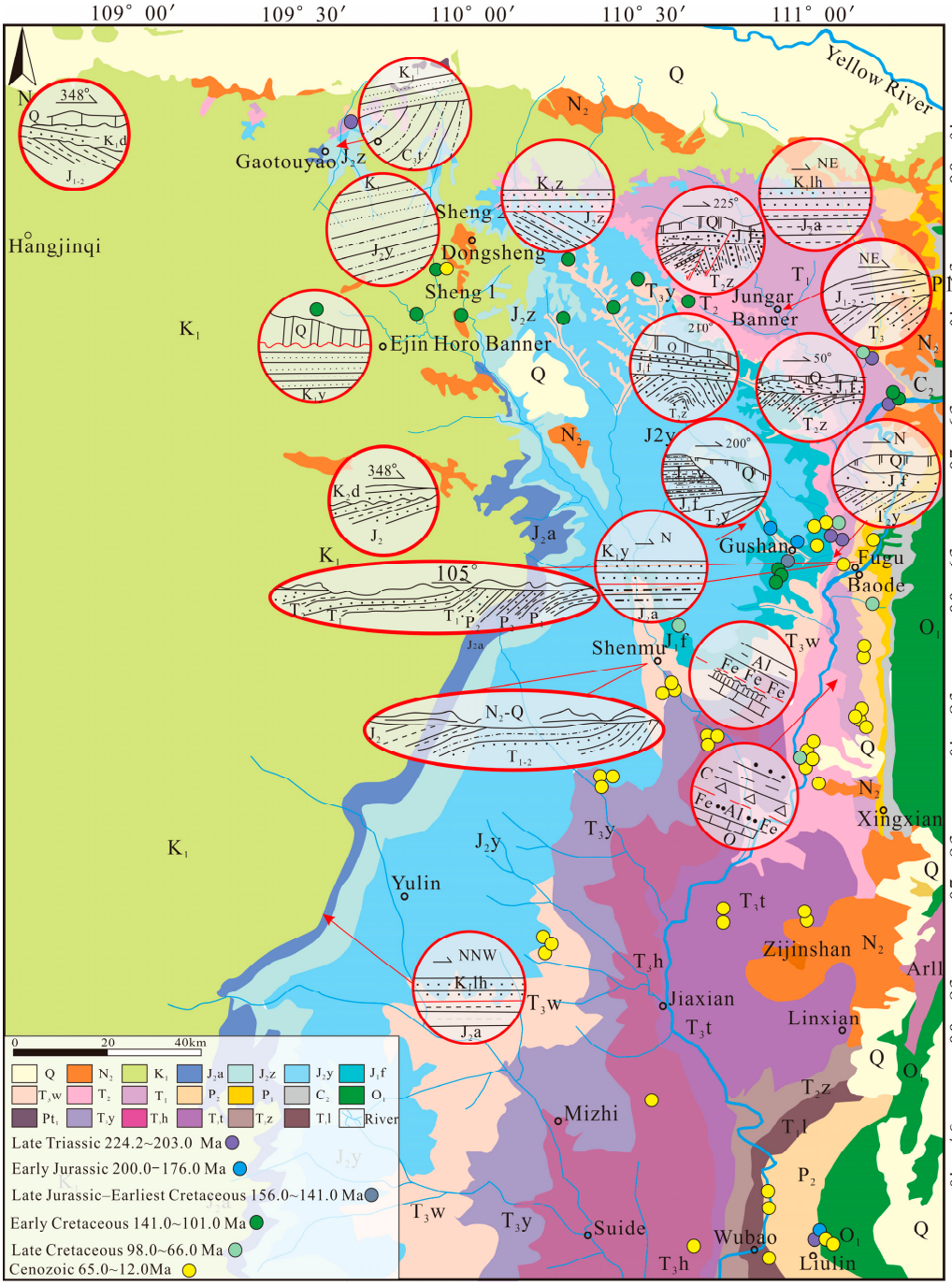


Figure 6. Distribution of low-temperature thermochronology data and unconformities in the northeastern Ordos Basin.

During the Late Cretaceous, the study area was generally in a stable uplift stage, consistent with the overall uplift of the Ordos Basin during the Late Cretaceous. Cretaceous strata exposed along the basin's northern margin dip gently northward. This observation

implies that late-stage evolution of the faulted basin in the Hetao area may have triggered localized subsidence along this margin, which could explain the present-day watershed geomorphology of the Yimeng Uplift along the Dongsheng–Hangjinqi. This uplift phase continued into the early Cenozoic, resulting in the widespread absence of Late Cretaceous–Paleogene strata in the northern part of the basin. During the late Cenozoic, accompanied by the Cenozoic rotation of the Ordos Block, NW-trending faults in the study area underwent obvious sinistral strike-slip movement. The Qingshuichuan Fault formed a transtensional fault zone under this background, which forms small graben structures in cross section.

5.3. Geodynamic Background and Significance of Uplift Events

The Early Mesozoic represents a critical interval for major reorganization of the tectonic framework and basin system of the Ordos Basin. During this period, the basin resided in a distinctive tectonic regime marked by bidirectional compressional convergence from its northern and southern margins. The Paleo-Tethys Ocean to the south of the Ordos Basin underwent its final subduction and closure [13], whereas the Paleo-Asian Ocean along the northern margin of the basin, after experiencing a scissor-like westward-to-eastward closure in the Late Paleozoic [64,65], finally closed during the Middle–Late Triassic [66]. The Middle–Late Triassic was also the main period of convergence and collision between the North China and South China continents, as well as the Qinling orogeny between them [67,68]. Consequently, previous studies have suggested that the Indosinian tectonic event had the most significant reworking effect on the southern part of the Ordos Basin, causing the first large-scale uplift in this area since the Mesozoic [69]. Far-field compressional stresses derived from collisional orogeny likely constituted the primary driver for Late Triassic–Early Jurassic tectonic uplift across the Ordos Basin, with uplift and exhumation intensity progressively decreasing toward the northeast [69]. However, this study reveals that the northeastern part of the Ordos Basin also experienced strong tectonic uplift and stratigraphic erosion during the Late Triassic. The NW-trending structural deformation in this region indicates that the regional principal stress field was oriented NE-SW. Therefore, the NE-SW compressional stress induced by the final closure and orogeny of the eastern Paleo-Asian Ocean controlled Late Triassic tectonic uplift in the northeastern Ordos Basin (Figure 7).

Since the Jurassic, the East Asian continent, including the Ordos Block, experienced another major tectonic event, namely the Yanshanian Movement [70,71]. The Yanshanian Movement can be divided into three core tectonic evolution stages: a main deformation period at 175~136 Ma, a main extension period at 135~90 Ma, and a weak compressional deformation period at 89~80 Ma [70,71]. This tectonic event has preserved distinct and continuous geological records within the Ordos Basin. During the Jurassic, nearly synchronous compressional convergence of the Paleo-Pacific, Mongol–Okhotsk, and Middle Tethys oceans toward East Asia established a regional multidirectional compressional stress regime (Figure 7) [70]. This tectonic setting triggered westward tilting and uplift of the basin's eastern domain, as well as intense intracontinental thrust-nappe deformation along its southwestern margin [14]. Large-scale thrust structures developed along the basin's western margin, whereas the eastern domain underwent sustained uplift and erosion, ultimately yielding a widespread unconformity between Middle Jurassic and Lower Cretaceous strata within the basin. Late Jurassic tectonic compression in the northern part of the basin was mainly manifested as southward tilting of strata and E-W trending small-amplitude folds, indicating a N-S compressional stress direction. The Yinshan Orogenic Belt along the northern margin of the basin also records contemporaneous N-S compressional structures, which are considered to be related to the Late Jurassic closure of the Mongol–Okhotsk Ocean [71,72].

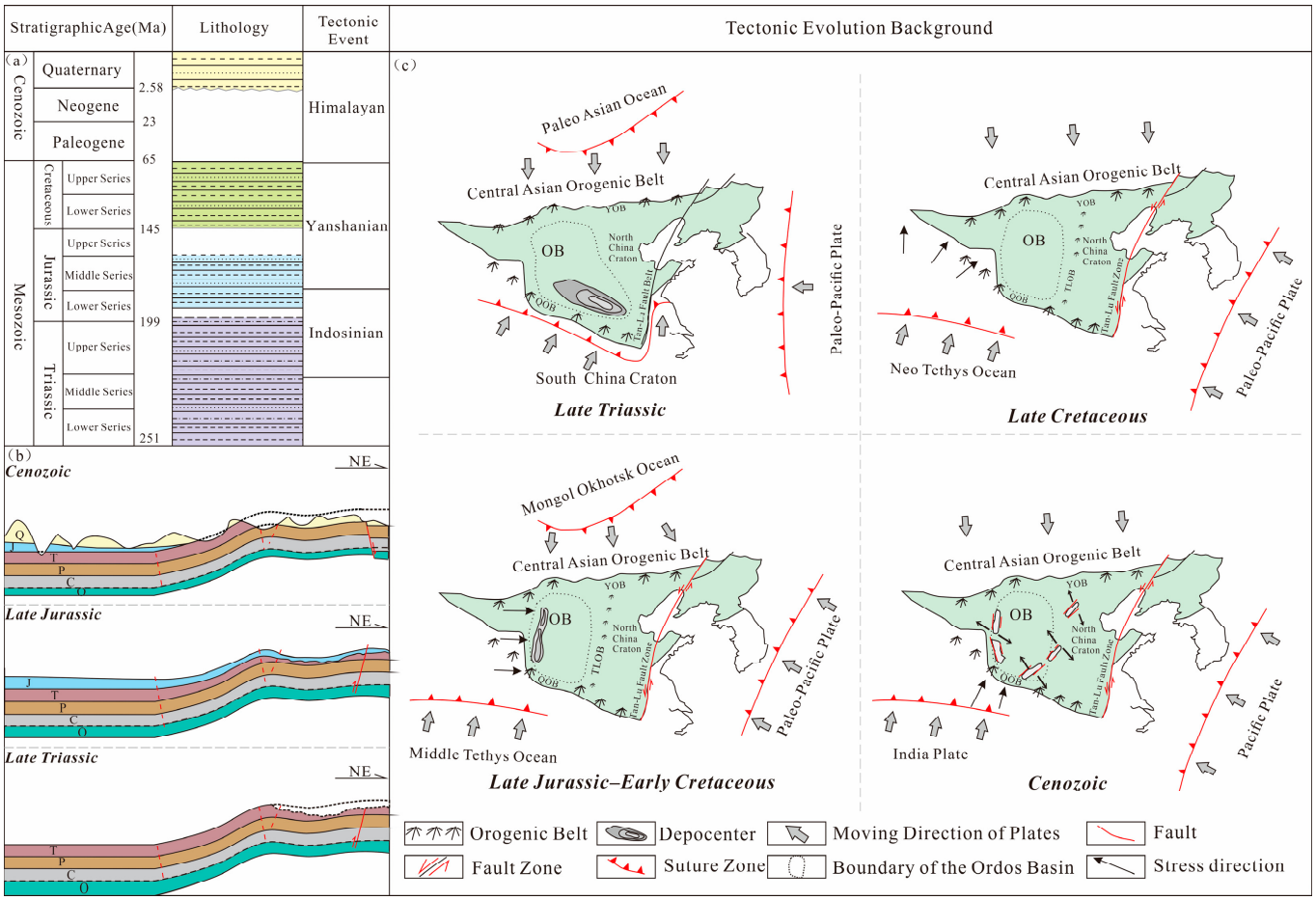


Figure 7. (**a**)Tectonic sequence of the northeastern Ordos Basin; (**b**) regional evolution of the OB and NCC in the Mesozoic–Cenozoic; (**c**) tectonic evolution model diagram of the northeastern Ordos Basin.

In the Early Cretaceous, the tectonic environment of the Ordos Block changed to weak extension, and the basin received thick Early Cretaceous Zhidan Group deposits. However, tectonic activity was markedly differentiated within the basin, with continued uplift in the east and persistent thrust activity in the west. In the Late Cretaceous, driven by combined effects of West Pacific Plate subduction, Neo-Tethys evolution (Figure 7), as well as the related deep continental geodynamic setting [2], the Ordos Block underwent regional uplift and erosion [14], resulting in the widespread absence of Upper Cretaceous and Paleogene strata in the basin. The parallel or low-angle unconformable contact between the Cretaceous and Paleogene indicates that this tectonic event was dominated by relatively stable overall uplift.

During the Cenozoic, subduction and convergence of the Pacific Plate and the India–Eurasia collision played a key role in shaping the tectonic and geomorphological framework of the East Asian continent. The most prominent Cenozoic tectonic feature of the Ordos Basin is the development of the "Circum-Ordos Cenozoic Rift System" surrounding the basin (Figure 7) [2,6,73]. The Ordos Basin is located at the intersection of the Pacific tectonic domain and the Tibetan Plateau tectonic domain and has been subjected to superimposed reworking by both [10]. From the latest Oligocene to the early Miocene, the Tibetan Plateau underwent a marked tectonic transition marked by episodic outward growth, which profoundly impacted adjacent terranes [74]. The adjacent Ordos Block also experienced strong NE-SW compression during the late Cenozoic [64]. Slab rollback and trench retreat driven by Pacific Plate subduction have been widely invoked to explain Cenozoic extension within the Ordos Block and even across the entire NCC [75–77]. Under the combined action of

these multiple regional geodynamic processes, the Ordos Block experienced counterclockwise rotation, facilitating the development of its peripheral rift system [6]. At present, several faults in the northeastern Ordos Basin still exhibit significant strike-slip activity [22]. The late Cenozoic low-temperature thermochronological records obtained in this study also document this tectonic event.

6. Conclusions

This study carries out systematic low-temperature thermochronology in the Fugu area, northeastern Ordos Basin, to reconstruct the Mesozoic tectonic uplift history of this region. Furthermore, we compile published low-temperature thermochronological data for the northeastern Ordos Basin and discuss the dynamic framework of successive tectonic events. The key findings are as follows:

(1) The obtained apatite fission-track and (U-Th)/He ages range from 156.0 ± 8.7 Ma to 182.9 ± 9.6 Ma and 33.58 ± 1.05 Ma to 76.19 ± 2.40 Ma, respectively. Thermal history modeling results identify two Mesozoic cooling-uplift episodes in the Fugu area: the Late Triassic and the Late Jurassic.

(2) Statistical low-temperature thermochronological data reveal that the northeastern Ordos Basin predominantly exhibits several uplift and exhumation events: Late Triassic (224.2~203.0 Ma), Late Jurassic–earliest Cretaceous (156.0~141.0 Ma), Late Cretaceous (98.0~66.0 Ma), and Paleogene–Neogene (65.0~12.0 Ma). The Late Cretaceous and Paleogene–Neogene events are inferred mainly from previously published regional thermochronological records and are not supported by our new dataset.

(3) The results show that Late Triassic uplift resulted from far-field superimposed compression associated with final closure of the northern Paleo-Asian Ocean; Late Jurassic uplift was linked to synchronous multi-directional plate convergence acting on the Ordos Block; Late Cretaceous weak regional uplift, jointly produced by the subduction of the West Pacific Plate and the Neo-Tethys Ocean, as well as the related deep continental geodynamic setting; and Paleogene–Neogene rapid exhumation was dominated by eastern Pacific Plate subduction, with additional far-field forcing from the northeastward tectonic propagation of the Tibetan Plateau.

Supplementary Materials: The following supporting information can be downloaded at: https://www.mdpi.com/article/10.3390/min16121246/s1, Table S1: AFT, ZFT, and U-Th-He age data from the northeastern Ordos Basin.

Author Contributions: Conceptualization, J.Z. and M.L.; methodology, J.Z. and C.J.; validation, S.C., L.L., and C.W.; investigation, L.L. and X.X.; data curation, C.W. and C.N.; writing—original draft preparation, J.Z., M.L., and X.Z.; writing—review and editing, X.Z. and L.X.; visualization, T.L. and Y.L.; supervision, X.Z. All authors have read and agreed to the published version of the manuscript.

Funding: This research was funded by the National Natural Science Foundation of China, grant numbers 41807190 and 42304152.

Data Availability Statement: The original contributions presented in this study are included in the article and Supplementary Materials. Further inquiries can be directed to the corresponding author.

Acknowledgments: We would like to express our gratitude to Lei Huang and Jianqiang Wang from Northwest University for their assistance in sampling. We are also grateful to the anonymous reviewers for their valuable comments and suggestions.

Conflicts of Interest: Junman Zhang, Ming Liang, Chuanwei Jia, Songsong Cheng, Lin Li, Chao Wang and Xiuyou Xu are employees of their respective commercial companies. This paper reflects the views of the authors and not those of the companies. The remaining authors declare that the research was

conducted in the absence of any commercial or financial relationships that could be construed as a potential conflict of interest.

References

1. Zhai, M.G. Ordos Block (Basin) is a key to understand early continental evolution and tectonic regime of the North China Craton. *Chin. Sci. Bull.* **2021**, *66*, 3441–3461. [CrossRef]
2. Liu, C.Y.; Zhao, H.G.; Gui, X.J.; Yue, L.P.; Zhao, J.F.; Wang, J.Q. Space-Time Coordinate of the Evolution and Reformation and Mineralization Response in Ordos Basin. *Acta Geol. Sin.* **2006**, *80*, 617–638.
3. Li, S.Z.; Li, X.Y.; Wang, G.Z.; Liu, Y.M.; Wang, Z.C.; Wang, T.S.; Cao, X.Z.; Guo, X.Y.; Somerville, I.; Li, Y.; et al. Global Meso-Neoproterozoic plate reconstruction and formation mechanism for Precambrian basins: Constraints from three cratons in China. *Earth Sci. Rev.* **2019**, *198*, 102946. [CrossRef]
4. Zhao, J.F.; Liu, C.Y.; Huang, L.; Zhang, D.D.; Wang, D.; Wang, D. Paleogeography reconstruction of a multi-stage modified intra-cratonic basin—A case study from the Jurassic Ordos Basin, western North China Craton. *J. Asian Earth Sci.* **2020**, *190*, 104191. [CrossRef]
5. He, D.F.; Bao, H.P.; Kai, B.Z.; Wei, L.B.; Xu, Y.H.; Ma, J.H.; Cheng, X. Critical tectonic modification periods and their geologic features of Ordos Basin and adjacent area. *Acta Pet. Sin.* **2021**, *42*, 1255–1269.
6. He, D.F.; Cheng, X.; Zhang, G.W.; Zhao, W.Z.; Zhao, Z.; Liu, X.; Bao, H.P.; Fan, L.Y.; Zou, S.; Kai, B.Z.; et al. Scope, nature, and exploration significance of Ordos Basin during geological historical periods, NW China. *Pet. Explor. Dev.* **2025**, *52*, 757–771. [CrossRef]
7. Peng, H.; Wang, J.Q.; Liu, C.Y.; Zhao, H.G.; Huang, L.; Zhao, X.C.; Zhang, S.H.; Liang, C.; Wang, Z.; Catto, S.; et al. Long-term and multiple stage exhumation of the Ordos Basin, western North China Craton: Insights from seismic reflection, borehole and geochronological data. *Earth Sci. Rev.* **2023**, *238*, 104349. [CrossRef]
8. Liu, C.Y.; Zhao, H.G.; Tan, C.Q.; Wang, J.Q. Occurrences of multiple energy mineral deposits and mineralization/reservoiring system in the basin. *Oil Gas Geol.* **2006**, *27*, 131–142.
9. Wang, S.M.; Zhao, X.C.; Sun, Q.; Geng, J.S.; Chen, Y.T.; Niu, C.; Wang, J.Q.; Shi, Q.M.; Li, J.T.; Ning, Z.G.; et al. Formation and evolution, coexistence characteristics, and geological support for loss-reducing mining of multiple energy resources in the Ordos Basin. *Geol. China* 2026 , *in press*.
10. Shi, W.; Dong, S.W.; Hu, J.M. Neotectonics around the Ordos Block, North China: A review and new insights. *Earth Sci. Rev.* **2020**, *200*, 102969. [CrossRef]
11. Peng, H.; Wang, J.; Liu, C.; Zhang, S.; Zattin, M.; Wu, N.; Feng, Q. Thermochronological constraints on the Meso-Cenozoic tectonic evolution of the Haiyuan-Liupanshan region, northeastern Tibetan Plateau. *J. Asian Earth Sci.* **2019**, *183*, 103966. [CrossRef]
12. Ju, Y.W.; Wang, W.; Ren, Z.L.; Yang, Z.; Liu, K.Y.; Hou, B.; Xiao, L. Multi-stage evolution of the Ordos Basin: Its coupled basin-mountain systems and energy resources. *Sci. China Earth Sci.* **2025**, *55*, 2537–2582. [CrossRef]
13. Xu, Y.H.; He, D.F.; Mao, D.F.; Cheng, C.Y. Types and distribution characteristics of the Indosinian unconformities in the Ordos Basin. *Acta Geol. Sin.* **2024**, *98*, 3630–3646.
14. Liu, H.; He, D.F.; Mao, D.F.; Zou, S. Types and distribution characteristics of Yanshanian unconformities in the Ordos Basin. *Acta Geol. Sin.* **2025**, *99*, 4053–4070.
15. Xiong, J.B.; He, D.F. Types and distribution characteristics of the Caledonian unconformities in the Ordos Basin. *J. Palaeogeogr.* **2022**, *24*, 970–988.
16. Wang, F.; Tian, J.C.; Fan, L.Y.; Chen, R.; Qiu, J. Evolution of sedimentary fillings in Triassic Yanchang Formation and its response to Indosinian Movement in Ordos Basin. *Nat. Gas Geosci.* **2010**, *21*, 882–889.
17. Yang, X.Y.; Dong, Y.P. Multiple phases of deformation in the southern Helanshan tectonic belt, northern China. *J. Asian Earth Sci.* **2020**, *201*, 104497. [CrossRef]
18. Zhang, S.H.; Liu, C.Y.; Yang, M.H.; Bai, J.K.; Wang, J.Q. Latest Triassic to Early Jurassic thrusting and exhumation in the southern Ordos Basin, North China: Evidence from LA-ICP-MS-based apatite fission track thermochronology. *Acta Geol. Sin.* **2018**, *92*, 1334–1348. [CrossRef]
19. Yu, Q.; Ren, Z.L.; Li, R.X.; Chung, L.; Tao, N.; Cui, J.P.; Wang, B.J.; Qi, K.; Khaled, A. Cooling history of the southwestern Ordos Basin (northern China) since Late Jurassic: Insights from thermochronology and geothermometry. *J. Asian Earth Sci.* **2021**, *219*, 104895. [CrossRef]
20. Zhao, X.C.; Wei, X.R.; Niu, Y.Z.; Chen, Y.T.; Li, D.L.; Du, F.P.; Jiang, Y.R.; Li, J.T.; Liu, Y.M.; Ning, Z.G. Meso-Cenozoic multi-stage tectono-thermal history reconstruction of the western Ordos Basin: A case study of the Weiningbeishan tectonic belt. *Geol. J.* 2026, *in press*. [CrossRef]
21. Peng, H.; Wang, J.Q.; Liu, C.Y.; Huang, L.; Zattin, M. Mesozoic exhumation and ca. 10 Ma reactivation of the southern Yin Shan, North China, revealed by low-temperature thermochronology. *Tectonophysics* **2022**, *823*, 229189. [CrossRef]

22. He, X.Y.; Liu, C.Y.; Zhang, L.; Wang, J.Q.; Huang, L.P.; Du, F.P.; Yang, X.K. The tectonic uplift episodes and energy effects in the northeastern Ordos Basin. *Acta Geol. Sin.* **2024**, *98*, 3735–3750.
23. Shi, J.; He, D.F.; Bao, H.P.; Wei, L.B. Tectonic analysis of the eastern boundary of Ordos Basin: A case study of the northern region of Shilou area. *J. Palaeogeogr.* **2024**, *26*, 150–164.
24. He, Z.X.; Fu, J.H.; Xi, S.L.; Fu, S.T.; Bao, H.P. Geological features of reservoir formation of Sulige gas field. *Acta Pet. Sin.* **2003**, *24*, 6–12.
25. Liang, J.W. Study on the Jurassic Sedimentary Systems and Sequence Stratigraphy in the Ordos Basin. Ph.D. Thesis, Northwest University, Xi'an, China, 2007.
26. Hao, S.M.; Li, L.; Zhang, W.; Qi, R.; Ma, C.; Chen, J.Y. Forming conditions of large-scale gas fields in Permo-Carboniferous in the northern Ordos Basin. *Oil Gas Geol.* **2016**, *37*, 149–154.
27. Liang, Q.S. Sedimentary Characteristics and Coupling Relationships of the Chang 7 Event Deposits in the Triassic Yanchang Formation, Ordos Basin. Ph.D. Thesis, Chengdu University of Technology, Chengdu, China, 2020.
28. Guo, G.S.; Xu, F.Y.; Liu, L.F.; Cai, Y.D.; Qin, W.; Chen, Z.H.; Deng, J.M.; Li, Z.L. Enrichment and accumulation patterns and favorable area evaluation of deep coalbed methane in the Fugu area, Ordos Basin. *Coal Geol. Explor.* **2024**, *52*, 81–91.
29. Farley, K.A.; Shuster, D.L.; Ketcham, R.A. U and Th zonation in apatite observed by laser ablation ICPMS, and implications for the (U–Th)/He system. *Geochim. Cosmochim. Acta* **2011**, *75*, 4515–4530. [CrossRef]
30. Flowers, R.M.; Ketcham, R.A.; Shuster, D.L.; Farley, K.A. Apatite (U-Th)/He thermochronometry using a radiation damage accumulation and annealing model. *Geochim. Cosmochim. Acta* **2009**, *73*, 2347–2365. [CrossRef]
31. Reiners, P.W.; Zhou, Z.; Ehlers, T.A.; Xu, C.; Brandon, M.T.; Donelick, R.A.; Nicolescu, S. Post-orogenic evolution of the Dabie Shan, eastern China, from (U-Th)/He and fission-track thermochronology. *Am. J. Sci.* **2003**, *303*, 489–518. [CrossRef]
32. Rohrmann, A.; Kapp, P.; Carrapa, B.; Reiners, P.W.; Guynn, J.; Ding, L.; Heizler, M. Thermochronologic evidence for plateau formation in central Tibet by 45 Ma. *Geology* **2012**, *40*, 187–190. [CrossRef]
33. Sun, J.B.; Qin, K.Z.; Chen, W.; Liu, Y.H.; Shen, Z.; Zhang, B.; Zhang, Z.Y.; Xing, L.; Zhao, S.F.; Zhang, W.; et al. Exhumation history of the Katebasu gold–copper deposit, Western Tianshan, NW China: Constraints from (U–Th)/He and fission-track thermochronology. *Ore Geol. Rev.* **2023**, *152*, 105220. [CrossRef]
34. Zhang, B.; Yang, J.; Chen, W.; Liu, J.Q.; Sun, Z.H.; Sun, J.B.; Zhou, Z.J. Inverted apatite fission track and (U-Th)/He ages reveal a two-stage evolution of the northwestern Tibetan Plateau. *Glob. Planet. Change* **2026**, *262*, 105492. [CrossRef]
35. Qiu, N.S.; Zuo, Y.H.; Chang, J.; Li, W.Z. Geothermal evidence of Meso-Cenozoic lithosphere thinning in the Jiyang sub-basin, Bohai Bay Basin, eastern North China Craton. *Gondwana Res.* **2014**, *26*, 1079–1092. [CrossRef]
36. Danišík, M.; Kuhlemann, J.; Dunkl, I.; Evans, N.J.; Székely, B.; Frisch, W. Survival of ancient landforms in a collisional setting as revealed by combined fission track and (U-Th)/He thermochronometry: A case study from Corsica (France). *J. Geol.* **2012**, *120*, 155–173. [CrossRef] [PubMed]
37. Mackintosh, V.; Kohn, B.; Gleadow, A.; Tian, Y. Phanerozoic morphotectonic evolution of the Zimbabwe Craton: Unexpected outcomes from a multiple low-temperature thermochronology study. *Tectonics* **2017**, *36*, 2044–2067. [CrossRef]
38. McInnes, B.I.; Evans, N.J.; McDonald, B.J.; Kinny, P.D.; Jakimowicz, J. Zircon U-Th–Pb–He double dating of the Merlin kimberlite field, Northern Territory, Australia. *Lithos* **2009**, *112*, 592–599. [CrossRef]
39. Chang, J.; Brown, R.W.; Yuan, W.; Li, W.; Que, Y.; Qiu, N. Mesozoic cooling history of the "Bachu Uplift" in the Tarim Basin, China: Constraints from zircon fission-track thermochronology. *Radiat. Meas.* **2014**, *67*, 5–14. [CrossRef]
40. Gleadow, A.J.W.; Duddy, I.R.; Green, P.F.; Hegarty, K.A. Fission track lengths in the apatite annealing zone and the interpretation of mixed ages. *Earth Planet. Sci. Lett.* **1986**, *78*, 245–254. [CrossRef]
41. Wolf, R.A.; Farley, K.A.; Kass, D.M. Modeling of the temperature sensitivity of the apatite (U–Th)/He thermochronometer. *Chem. Geol.* **1998**, *148*, 105–114. [CrossRef]
42. Farley, K.A. (U-Th)/He dating: Techniques, calibrations, and applications. *Rev. Mineral. Geochem.* **2002**, *47*, 819–844. [CrossRef]
43. Tian, Y.; Kohn, B.P.; Gleadow, A.J.W.; Hu, S. A thermochronological perspective on the morphotectonic evolution of the southeastern Tibetan Plateau. *J. Geophys. Res. Solid Earth* **2014**, *119*, 676–698. [CrossRef]
44. Zhang, G.H.; Tian, Y.T.; Li, R.; Shen, X.M.; Zhang, Z.J.; Sun, X.L.; Chen, D.X. Progressive tectonic evolution from crustal shortening to mid-lower crustal expansion in the southeast Tibetan Plateau: A synthesis of structural and thermochronological insights. *Earth Sci. Rev.* **2022**, *226*, 103951. [CrossRef]
45. Gleadow, A.J.W. Fission-track dating methods: What are the real alternatives? *Nucl. Tracks* **1981**, *5*, 3–14. [CrossRef]
46. Gleadow, A.J.W.; Gleadow, S.J.; Belton, D.X.; Kohn, B.P.; Krochmal, M.S.; Brown, R.W. Coincidence mapping—A key strategy for the automatic counting of fission tracks in natural minerals. *Geol. Soc. Lond. Spec. Publ.* **2009**, *324*, 25–36. [CrossRef]
47. Farley, K.A.; Wolf, R.A.; Silver, L.T. The effects of long alpha-stopping distances on (U-Th)/He ages. *Geochim. Cosmochim. Acta* **1996**, *60*, 4223–4229. [CrossRef]
48. Sun, J.B.; Chen, W.; Yu, S.; Shen, Z.; Tian, Y.T. Study on zircon (U-Th)/He dating technique. *Acta Petrol. Sin.* **2017**, *33*, 1947–1956.

49. Green, P.F.; Crowhurst, P.V.; Duddy, I.R.; Apsen, P.; Holford, S.P. Conflicting (U-Th)/He and fission track ages in apatite: Enhanced He retention, not anomalous annealing behaviour. *Earth Planet. Sci. Lett.* **2006**, *250*, 407–427. [CrossRef]
50. Flowers, R.M.; Shuster, D.L.; Wernicke, B.P. Radiation damage control on apatite (U-Th)/He dates from the Grand Canyon region, Colorado Plateau. *Geology* **2007**, *35*, 447–450. [CrossRef]
51. Shuster, D.L.; Flowers, R.M.; Farley, K.A. The influence of natural radiation damage on helium diffusion kinetics in apatite. *Earth Planet. Sci. Lett.* **2006**, *249*, 148–161. [CrossRef]
52. Vermeesch, P.; Seward, D.; Latkoczy, C.; Wipf, M.; Günther, D.; Baur, H. α-Emitting mineral inclusions in apatite, their effect on (U-Th)/He ages, and how to reduce it. *Geochim. Cosmochim. Acta* **2007**, *71*, 1737–1746. [CrossRef]
53. Spiegel, C.; Kohn, B.; Belton, D.; Berner, Z.; Gleadow, A. Apatite (U-Th-Sm)/He thermochronology of rapidly cooled samples: The effect of He implantation. *Earth Planet. Sci. Lett.* **2009**, *285*, 105–114. [CrossRef]
54. Gautheron, C.; Barbarand, J.; Ketcham, R.A.; Tassan-Got, L.; Beek, P.; Pagel, M.; Jamme, R.P.; Couffignal, F.; Fialin, M. Chemical influence on α-recoil damage annealing in apatite: Implications for (U-Th)/He dating. *Chem. Geol.* **2013**, *351*, 257–267. [CrossRef]
55. Brown, R.W.; Beucher, R.; Roper, S.; Persano, C.; Stuart, F.; Fitzgerald, P. Natural age dispersion arising from the analysis of broken crystals. Part I: Theoretical basis and implications for the apatite (U-Th)/He thermochronometer. *Geochim. Cosmochim. Acta* **2013**, *122*, 478–497. [CrossRef]
56. Pearson, R. *Exploring Data in Engineering, the Sciences, and Medicine*; Oxford University Press: Oxford, UK, 2011.
57. Guenthner, W.R.; Reiners, P.W.; Ketcham, R.A.; Nasdala, L.; Giester, G. Helium diffusion in natural zircon: Radiation damage, anisotropy, and the interpretation of zircon (U-Th)/He thermochronology. *Am. J. Sci.* **2013**, *313*, 145–198. [CrossRef]
58. Farley, K.A. Helium diffusion from apatite: General behavior as illustrated by Durango fluorapatite. *J. Geophys. Res. Solid Earth* **2000**, *105*, 2903–2914. [CrossRef]
59. Ketcham, R.A.; Gautheron, C.; Tassan-Got, L. Accounting for long alpha-particle stopping distances in (U–Th–Sm)/He geochronology: Refinement of the baseline case. *Geochim. Cosmochim. Acta* **2011**, *75*, 7779–7791. [CrossRef]
60. Ketcham, R.A. Forward and Inverse Modeling of Low-Temperature Thermochronometry Data. *Rev. Mineral. Geochem.* **2005**, *58*, 275–314. [CrossRef]
61. Wang, S.Y.; Cheng, Y.H.; Li, C.H.; Li, Y.F.; Zhang, T.F.; Cheng, X.Y.; Yang, J. Tectonic evolution and its controls on the sandstone-type uranium mineralization in the Yimeng Uplift: Constraints from apatite fission track thermochronology. *Geotecton. Metallog.* **2020**, *44*, 682–696.
62. Ren, Z.L. Thermal history of Ordos Basin assessed by apatite fission-track analysis. *Chin. J. Geophys.* **1995**, *38*, 339–349.
63. Zhao, M.W.; Behr, H.J. Vitrinite reflectance in Triassic with relation to geothermal history of Ordos Basin. *Acta Pet. Sin.* **1996**, *17*, 15–23.
64. Wu, D.D.; Li, S.; Chew, D.; Liu, T.Y.; Guo, D.H. Permian-Triassic magmatic evolution of granitoids from the southeastern Central Asian Orogenic Belt: Implications for accretion leading to collision. *China Earth Sci.* **2021**, *64*, 788–806. [CrossRef]
65. Xue, J.X.; Cai, K.D.; Zhang, Z.J.; Wang, K. Timing and style of final closure of the Paleo-Asian Ocean: Perspectives from the big geodata analysis and machine learning model. *J. Geophys. Res. Solid Earth* **2025**, *130*, e2024JB029877. [CrossRef]
66. Song, D.F.; Xiao, W.J.; Windley, B.F.; Mao, Q.G.; Ao, S.J.; Wang, H.Y.C.; Li, R. Closure of the Paleo-Asian Ocean in the Middle-Late Triassic (Ladinian-Carnian): Evidence from provenance analysis of retroarc sediments. *Geophys. Res. Lett.* **2021**, *48*, e2021GL094276. [CrossRef]
67. Zhang, G.W.; Dong, Y.P.; Yao, A.P. Review on the development of studies on the tectonic and orogen process of orogenic belt, and discussing on some new key problems. *Northwest. Geol.* **2001**, *34*, 1–9.
68. Dong, Y.P.; Yang, Z.; Liu, X.M.; Sun, S.S.; Li, W.; Cheng, B.; Zhang, F.F.; Zhang, X.N.; He, D.F.; Zhang, G.W. Mesozoic intracontinental orogeny in the Qinling Mountains, central China. *Gondwana Res.* **2016**, *30*, 144–158. [CrossRef]
69. Wang, J.Q.; Liu, C.Y.; Zhao, H.G.; Zhang, D.D.; Zattin, M.; Peng, H. Uplift and exhumation events and thermochronological constraints at the end of the Triassic in southwestern Ordos Basin. *Acta Petrol. Sin.* **2020**, *36*, 1199–1212. [CrossRef]
70. Dong, S.W.; Zhang, Y.Q.; Long, C.X.; Yang, Z.Y.; Ji, Q.; Wang, T.; Hu, J.M.; Chen, X.H. Jurassic tectonic revolution in China and new interpretation of the Yanshan Movement. *Acta Geol. Sin.* **2007**, *81*, 1449–1461.
71. Dong, S.W.; Zhang, Y.Q.; Li, H.L.; Shi, W.; Xue, H.M.; Li, J.H.; Huang, S.Q.; Wang, Y.C. The Yanshan orogeny and late Mesozoic multi-plate convergence in East Asia—Commemorating 90th years of the "Yanshan Orogeny". *China Earth Sci.* **2019**, *49*, 913–938.
72. Davis, G.A.; Cong, W.; Zheng, Y.D.; Zhang, J.J.; Zhang, C.H.; Gehrels, G.E. The enigmatic Yinshan fold-and-thrust belt of northern China: New views on its intraplate contractional styles. *Geology* **1998**, *26*, 43–46. [CrossRef]
73. Gong, W.B.; Hu, J.M.; Chen, H.; Li, Z.H.; Qu, H.J.; Yang, Y. Late Mesozoic tectonic evolution and kinematic mechanisms in the Daqing Shan at the northern margin of the North China Craton. *J. Asian Earth Sci.* **2015**, *114*, 103–114. [CrossRef]
74. Deng, Q.D.; Cheng, S.P.; Min, W.; Yang, G.Z.; Ren, D.W. Discussion on Cenozoic tectonics and dynamics of Ordos Block. *J. Geomech.* **1999**, *5*, 13–21.
75. Liu, C.Y.; Zhao, H.G.; Zhang, C.; Wang, J.Q. The important turning period of evolution in the Tibet-Himalayan tectonic domain. *Earth Sci. Front.* **2009**, *16*, 1–12.

76. Zhang, Y.Q. Cenozoic movement history and tectonic stress regime transition of the Qinling fault system and the southern segment of the Tan-Lu fault zone. *Acta Geol. Sin.* **1999**, *73*, 286.
77. Zhang, Y.Q.; Yang, N.; Chen, W.; Ma, Y.S.; Meng, H. Late Cenozoic tectonic deformation history of the East-West geomorphological boundary zone of China and uplift process of the eastern margin of the Tibetan Plateau. *Earth Sci. Front.* **2003**, *10*, 599–612.

Disclaimer/Publisher's Note: The statements, opinions and data contained in all publications are solely those of the individual author(s) and contributor(s) and not of MDPI and/or the editor(s). MDPI and/or the editor(s) disclaim responsibility for any injury to people or property resulting from any ideas, methods, instructions or products referred to in the content.